Destroy, create, transform and sublimate: laboratory dissociation studies on polycyclic aromatic hydrocarbons and analogues

Kamer, J.

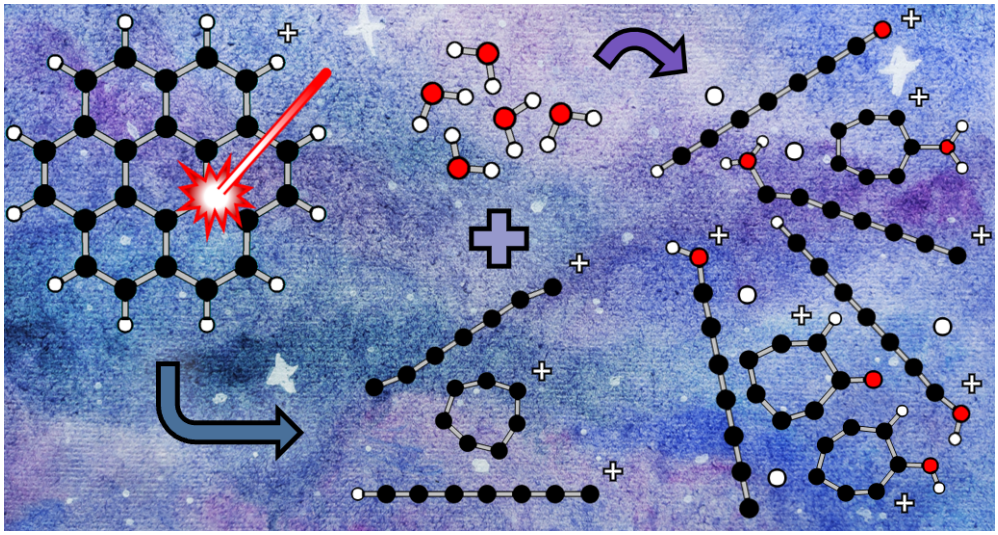

6 Reactions of Coronene$^{\bullet+}$ Photodissociation Fragment Ions with Water in a room-temperature Quadrupole Ion Trap

Polycyclic aromatic hydrocarbons (PAHs) are present in a wide variety of interstellar environments. Only large PAHs can survive in the harsh radiation fields in photon dominated regions and small PAHs photodissociate. Although the (photo)dissociation mechanisms of PAHs are quite well understood, the formed reaction products' structures and their further reaction with closed-shell species remain to be investigated. In this work, we study the reactivity of room-temperature coronene$^{\bullet+}$ photodissociation fragments by mass-selectively isolating the $C_{11}{}^{\bullet+}$, $C_{10}{}^{\bullet+}$, C_9H^+, $C_9{}^{\bullet+}$, C_7H^+, $C_7{}^{\bullet+}$ and C_5H^+ fragment ions and subsequently reacting them with gas-phase water. Furthermore, a resonant ejection technique is applied to elucidate the chemical link between the C_9H^+, $C_9{}^{\bullet+}$, C_7H^+ and $C_7{}^{\bullet+}$ reactants and reaction products. Several fragments are found to react with water and some of the formed reaction products stabilize by the loss of atomic hydrogen or CO. Some differences in fragment reactivity are observed and we argue that these may be explained by the (cyclic vs. linear) geometry of the coronene$^{\bullet+}$ dissociation fragments. Reaction mechanisms for the cyclic and linear $C_7{}^{\bullet+}$ isomers reacting with water, based on potential energy surface (PES) calculations, are presented to rationalize the experimental findings. Lastly, the role that dissociation fragments of small interstellar PAHs play in the chemical evolution of carbonaceous material in the interstellar medium (ISM) is discussed.

Kamer, J., Bouwman, J., 2025, ACS Earth and Space Chemistry, 9, 1017-1029.
Part of ACS Earth and Space Chemistry special issue "Harold Linnartz Festschrift".

6.1 Introduction

Mid-infrared (mid-IR) emission features in the $3 - 20$ μm spectral region are observed towards a variety of interstellar objects (Tielens 2008). These features are attributed Polycyclic Aromatic Hydrocarbons (PAHs) that are excited by the interstellar radiation field and subsequently decay to the ground state by emitting IR radiation at wavelengths of 3.3, 6.2, 7.7, 8.6, 11.2 and 12.7 μm that correspond to their characteristic vibrational modes (Leger & Puget 1984; Allamandola *et al.* 1985, 1989). PAHs are found to be ubiquitous and it has been estimated that up to 20% of all elemental carbon in the universe is locked-up in these molecular species (Tielens 2008). For decades, interstellar PAHs were only identified as a family of molecules. This changed recently with the first unambiguous detections of PAHs through radio astronomical observations of the cold and quiescent Taurus molecular cloud (McGuire *et al.* 2021; Wenzel *et al.* 2024, 2025; Burkhardt *et al.* 2021a).

Only PAHs with more than ~ 50 carbon are expected to be stable enough to survive the harsh radiation in photon dominated regions, and smaller PAH species are expected to photodissociate (Allamandola *et al.* 1989; Allain *et al.* 1996; Andrews *et al.* 2015). The photodissociation mechanisms of PAH cations have been studied in detail and Harold Linnartz and co-workers found that large PAHs (N_C with $\mathrm{C} \geq 34$) tend to first lose all of their hydrogen atoms in pairs and then break down further by loss of C_2 units (Zhen *et al.* 2014a,b; Hrodmarsson *et al.* 2023). Dissociation of smaller PAHs (N_C with $16 < \mathrm{C} \leq 24$), on the other hand, generally proceeds via H loss, H_2 loss, CH loss and C_2H_2 loss (Panchagnula *et al.* 2020; Bouwman *et al.* 2016; Panchagnula *et al.* 2024; Castellanos, P. *et al.* 2018; West *et al.* 2019, 2014a,b; Trinquier *et al.* 2017; Holm *et al.* 2011; Zhen *et al.* 2014a; Ekern *et al.* 1998), ultimately forming bare ionic carbon chains and rings: $C_n{}^{\bullet+}$ with $n = 10 - 15$. The formation of the latter species appears to be independent of the symmetry of the parent ion (Panchagnula *et al.* 2024; Hrodmarsson *et al.* 2022, 2023), and of five-membered ring inclusion (Sundararajan *et al.* 2024) or exoskeletal nitrogen atom substitution (Schleier *et al.* 2024a) in the parent ion. A few studies extended into the low-mass range of the mass spectrum (Panchagnula *et al.* 2024; Sundararajan *et al.* 2024; Schleier *et al.* 2024a) ($m/z < 120$) and, also here, similar daughter ions were identified for varying PAH structures. In this mass range, however, the dominant fragments are generally protonated, e.g., C_9H^+, C_7H^+ and $C_7H_3{}^+$. Based on the appearance of peculiar peaks in the mass spectra of these photodissociation studies, it was suggested that certain PAH dissociation fragments undergo subsequent reactions inside the ion trap (Panchagnula *et al.* 2024; Sundararajan *et al.* 2024; Schleier *et al.* 2024a). Such subsequent reactions involving dissociation fragments formed by photodissociating small PAHs may also occur in the ISM and must be investigated in detail. Previous studies have demonstrated that benzene and PAH radicals react with neutral molecules such as water and methanol, and the binding energies of the thus formed clusters were determined (Ibrahim *et al.* 2005; Attah *et al.* 2014).

Gas-phase reactions between cationic carbon clusters and neutral reactants have been extensively studied by McEvalny and co-workers in the 1980s. The cationic carbon species as well as their protonated analogues were formed using Nd:YAG laser ablation of a graphite rod and these species were subsequently reacted with D_2 (McElvany *et al.* 1987), CH_4, C_2H_2, C_2H_4 (McElvany 1988) and HCN gas (Parent & McElvany 1989). The ions were stored and reacted with a Fourier Transform Ion Cyclotron Resonance (FTICR) mass spectrometer. Branching ratios were determined for these reactions, from which it was derived that the reactions involving $C_n{}^{\bullet+}$ with $n \leq 9$ generally proceed via addition of the reactant followed by the loss of a hydrogen (or deuterium) atom. Species with $n \geq 10$ were found to not lose a hydrogen atom after the reaction, or they were found to not react at all. The reaction of the protonated species (C_mH^+) with HCN and C_2H_2 both proceeded via addition followed by hydrogen loss for even values of m and no hydrogen atom was lost for odd values of m. The reaction of C_5H^+ with C_2H_2 was found to proceed via addition, followed by the hydrogen

atom loss, while the reaction with HCN showed no subsequent loss of a hydrogen atom. A study of the gas-phase reactions of C_3H^+ in a selected-ion flow tube reactor revealed that the addition of water to the ion can also be followed by the loss of CO (Raksit & Bohme 1983).

McEvalny and co-workers tried to determine the structure of the $C_n{}^{\bullet+}$ carbon cluster ions and suggested that a change in the cluster ion geometry from linear to cyclic takes place between $n = 9$ and 10. Further research on the geometry of carbon cluster ions was done by Von Helden and co-workers in the 1990s. They formed carbon cluster ions and protonated carbon clusters by the excimer laser ablation of a carbon rod and studied their geometry using ion mobility measurements. They found $C_n{}^{\bullet+}$ clusters to be entirely monocyclic for $n = 11 - 20$, a finding that has been confirmed again more recently, (Marlton *et al.* 2023; Buntine *et al.* 2021) while species with $n = 7-10$ were found to exist in both a monocyclic and linear geometry with varying ratios depending on the experimental conditions. Small species with $n = 3-6$ were found to be fully linear (von Helden *et al.* 1993; von Helden *et al.* 1993a,b, 1994), although more recent works have shown $C_6{}^{\bullet+}$ can be created in both the linear and cyclic configuration through different formation processes (Colley *et al.* 2022; Campbell & Dunk 2019). Because of their interstellar relevance and their potential contribution to the diffuse interstellar bands, many of these pure carbon cluster species have also been subjected to spectroscopic studies, as well as studies of their dissociation characteristics (Rohlfing *et al.* 1984; Geusic *et al.* 1987; Kohno *et al.* 1998; Fulara *et al.* 2004, 2005; Chen *et al.* 2014; Marlton *et al.* 2023; Colley *et al.* 2022; Rademacher *et al.* 2022; Ferrari *et al.* 2023). The protonated carbon clusters were found to have either have monocyclic or linear geometries. C_mH^+ species with $m = 10 - 22$ are predominantly cyclic and C_9H^+ exists almost entirely in a linear configuration (Lee *et al.* 1997).

In this work, the reactivity of coronene$^{\bullet+}$ (**Cor**$^{\bullet+}$) photodissociation fragments is studied by mass-selectively isolating the $C_{11}{}^{\bullet+}$, $C_{10}{}^{\bullet+}$, C_9H^+, $C_9{}^{\bullet+}$, C_7H^+, $C_7{}^{\bullet+}$ and C_5H^+ fragment ions, which are among the most prominent PAH fragments found in previous studies (Zhen *et al.* 2014a,b; Hrodmarsson *et al.* 2023; Panchagnula *et al.* 2020; Bouwman *et al.* 2016; Panchagnula *et al.* 2024; Castellanos, P. *et al.* 2018; Hrodmarsson *et al.* 2022; Sundararajan *et al.* 2024; Schleier *et al.* 2024a), and detecting reaction reaction products formed by reacting these ions with gas-phase water in a room-temperature ion trap. Moreover, a resonant ejection technique that has been used in the past to disentangle reaction networks in ion traps (Fulford *et al.* 1980; Ardanaz *et al.* 1991; Kumondai *et al.* 2005) is applied to the C_9H^+, $C_9{}^{\bullet+}$, C_7H^+ and $C_7{}^{\bullet+}$ ions in order to unambiguously link the reaction products to specific dissociation fragment ions, therefore, allowing one to discriminate between direct **Cor**$^{\bullet+}$ photodissociation products and subsequent reaction products. We show that some **Cor**$^{\bullet+}$ fragments are extremely reactive and give rise to various reaction products. The reactions are compared to previous works, and differences in reactivity of ions are explained by considering their geometry. Reaction pathways for the reactivity of one of the main photodissociation fragments, $C_7{}^{\bullet+}$, are presented to rationalize the experimental results. Lastly, we put our results into an astrophysical context.

6.2 Methods

6.2.1 Experimental

The experimental work is conducted on our Instrument for the Photodissociation/Photodynamics of PAHs (i-PoP) located in the Laboratory for Astrophysics at the Leiden Observatory, Leiden University. The apparatus has been described extensively in the past (Zhen *et al.* 2014a), and here we only provide a concise overview of the instrument.

The apparatus consists of a main vacuum chamber that holds a commercial Paul-type quadrupole ion-trap (QIT, Jordan C-1251), at room-temperature, that is connected via a 2 mm skimmer to a reflectron time-of-flight (TOF) mass spectrometer system (Jordan C-

855, C-852, C-679 and C-701). A small quantity (about 1 mg) of commercially available coronene ($C_{24}H_{12}$, Sigma Aldrich, 97% purity) is placed in a ceramic oven (Heat Wave Labs) that is mounted inside the vacuum chamber next to the ion trap and heated to 130 °C to gently sublimate the PAH sample. The neutral coronene molecules that sublimated reach the ionization region, where they are electron ionized by 70 eV electrons from an electron gun (Jordan C-950). Electrostatic lenses subsequently guide the ions into the QIT through an ion gate that controls the filling time.

A 952 kHz radio frequency (RF) voltage is applied to the ring electrode of the QIT, resulting in a time-varying electric field that traps the ions. The peak-peak amplitude of the RF voltage (V_{RF}) can be adjusted to trap ions in a specific mass range (March 1997). A small continuous flow of helium gas is admitted directly into the ceramic housing of the QIT, until a static pressure of $1-2\times10^{-6}$ mbar is reached in the main vacuum chamber. Collisions with the helium gas allow the ions in the room-temperature trap to cool translationally, resulting in a confined ion cloud and a higher mass resolution $\left(\frac{m}{\Delta m}\right)$ when the ions are ejected from the trap. The QIT is filled for 2.7 s, after which an ion gate inhibits ions from entering the QIT.

After filling, the ions are exposed to laser light from a dye laser (LIOP-TEC, Quasar2-VN) that is pumped by a 10 Hz Nd:YAG laser (INDI-40-10). The dye was 4-(dicyanomethylene)-2-methyl-6-(4-dimethylaminostyryl)-4H-pyran (DCM) dissolved in ethanol, which allowed us to tune the laser to a wavelength of 630 nm. Irradiation of the ions at this wavelength ensures a multiphoton dissociation process, resulting in gently ramping up of the $\mathbf{Cor}^{\bullet+}$ internal energy to reach its dissociation threshold. Another advantage of this wavelength is the absence of processes such as multiphoton ionization, which do occur in experiments on PAHs of similar size to coronene when utilizing VUV radiation (Zhen *et al.* 2016; Wenzel *et al.* 2020). The laser exposure of 10 pulses per ion trap fill is controlled by a mechanical shutter. The average laser pulse energy is measured outside of the vacuum chamber after passing through the ion trap. A Stored Waveform Inverse Fourier Transform (Doroshenko & Cotter 1996) (SWIFT) pulse is applied during or after the irradiation of the ion cloud to the repeller endcaps to expel or retain our ions in a selected mass range of interest at a selected V_{RF}. Details on the laser pulse energy and SWIFT frequencies are reported in table 6.2.

Following the SWIFT pulse, the mass-selected ions are given time to react with background water in the room-temperature ion trap. Thereafter, the left over parent ions and (reaction) product ions are extracted from the trap by applying a potential of about +800 and −800 V to the repeller and extractor endcaps, respectively, accelerating the trap contents into the reflectron time-of-flight (re-TOF) tube. The ions are detected at the end of the flight tube using a multichannel plate (MCP) detector and signals are digitized using an 8 bit GaGe Cobra card with a bandwidth of 500 MHz. We run the data acquisition sequence via a LabView routine that controls two high-precision delay generators (SRS DG535) via a GPIB interface. The measurement cycle is triggered on the Q-switch of the Nd:YAG laser to ensure that the correct number of laser pulses is applied to the ion cloud for each individual measurement. Each mass spectrum presented in this chapter is the result of co-adding 50 individual mass spectra.

To quantitatively assess the data, each peak is fitted with a Pearson type IV distribution (Pearson 1895), which accounts for asymmetries. The fits are subsequently integrated numerically, resulting in the integrated intensity of the specific peak. All integrated peak signals are normalized to the most intense peak in a m/z range or to the peak of interest. Our measurement technique (see the next section) does not allow for the first-order correction of ^{13}C contributions of neighboring peaks, as the mass signals are affected by the SWIFT pulse, which causes the intensities to deviate from the natural abundance.

6.2.1.1 Resonant ejection using a V_{RF} sweep

For a *grounded* QIT, such as the one used in this work, ions remain on a stable trajectory in the trap if the stability parameter $\beta_z \leq 1$, where β_z is defined as (March 1997)

$$\beta_z^2 = \frac{{q_z}^2}{(\beta_z+2)^2 - \frac{{q_z}^2}{(\beta_z+4)^2 - \frac{{q_z}^2}{(\beta_z+6)^2-\ldots}}} + \frac{{q_z}^2}{(\beta_z-2)^2 - \frac{{q_z}^2}{(\beta_z-4)^2 - \frac{{q_z}^2}{(\beta_z-6)^2-\ldots}}}. \tag{6.1}$$

The parameter q_z is a Mathieu equation parameter, which follows from the properties of the QIT, and is given by (March 1997)

$$q_z = \frac{4eV_{\mathrm{RF}}}{m\,({r_0}^2 + 2{z_0}^2)\,\Omega^2}, \tag{6.2}$$

where e is the elementary charge, m is the mass of the ion of interest, r_0 is the ring electrode radius (1 cm in our system), z_0 is half the distance between the two-end cap electrodes (0.707 cm in our trap) and Ω represents the angular frequency of the RF voltage, which is about $5.98 \cdot 10^6$ rad s^{-1}. Because the geometry of the QIT and Ω are fixed, the value of q_z for a specific mass, m ($q_{z,m}$), is only linearly dependent on V_{RF}. Moreover, as β_z is only dependent on q_z, the mass specific β_z ($\beta_{z,m}$) is, thus, dependent on V_{RF}, such that a decrease/increase in V_{RF} results in a decrease/increase of the $\beta_{z,m}$ value.

The ions retained in the QIT follow a Lissajous curve trajectory of which the fundamental secular frequency $\omega_{z,m}$ is given by (March 1997)

$$\omega_{z,m} = \frac{1}{2}\beta_{z,m}\Omega. \tag{6.3}$$

The dependence of $\beta_{z,m}$ on V_{RF} shows that the secular frequencies of the (fragment) ions in the trap can be altered by changing V_{RF}.

In this work, we present measurements to distinguish between direct dissociation fragments of $\mathbf{Cor}^{\bullet+}$ and subsequent reaction products formed in the trap. To this end, we make use of two different measurement techniques and Fig. 6.1 shows schematic representation of the two used measurement cycles. For the first measurements, we create a SWIFT pulse that eliminates all dissociation fragments but a select series of specific dissociation fragments within a mass range of about 3 amu wide after irradiation (i.e., formation of the ions). Next, we monitor how these product species subsequently react in the trap with water to form reaction products. For the second measurement series, we create a SWIFT pulse that resonantly ejects only a small series of fragment ions (e.g., $C_7^{\bullet+}$, C_7H^+ and $C_7H_3^{\bullet+}$) from the trap at a specific V_{RF} during irradiation by exciting a range of secular frequencies corresponding to the masses of those fragments. This SWIFT pulse is constructed such, that none of the ions in the trap are affected at V_{RF} that is 50 V lower or 50 V higher. By stepping through this V_{RF} range, we essentially sweep over the fundamental secular frequency (see eqs. 6.1 – 6.3), and we can match the fundamental secular frequencies of the ions of interest with the SWIFT pulse, thus removing those from the trap. By stepping through the V_{RF}, we selectively remove these ions from the trap, allowing us to observe how their subsequently formed reaction products also disappear from the trap and hence link species chemically. This results in a measurement technique that distinguishes between fragment ions that originate from the dissociation of the parent ion directly from fragment ions that are (in part) formed from subsequent reactions with water in the ion trap.

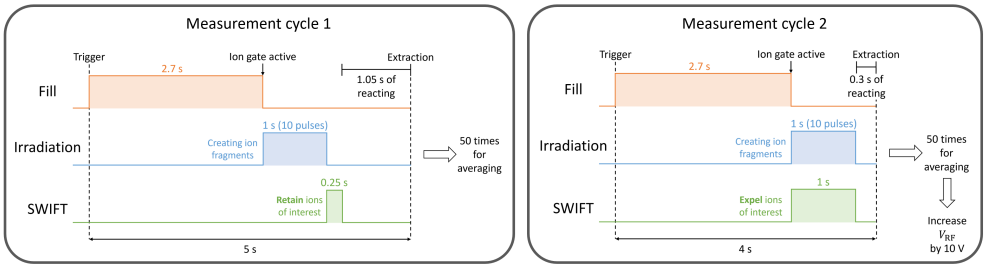

Figure 6.1: Schematic representation of the two measurement cycles used to study the reactivity of dissociation fragments (measurement cycle 1) and to perform resonant ejection (measurement cycle 2).

6.2.2 Computational

Density functional theory (DFT) calculations are performed using the Gaussian16 program (Frisch *et al.* 2016) in order to find the lowest energy structures of our experimentally detected fragment ions. Moreover, we explore the potential energy surface (PES) using B3LYP/6-311++G(d,p) to characterize potential formation mechanisms for the ions that are found to be formed in our ion trap by the reaction with gas-phase water.

6.3 Results and discussion

In this section, we first show how the $\mathbf{Cor}^{\bullet+}$ dissociation mass spectra depend on the V_{RF} used to trap the ions. Next, we mass select ions and show how they react with water inside the ion trap at room-temperature. Subsequently, we step the V_{RF} while keeping the same SWIFT isolation pulse over the mass range of interest to determine the exact chemical origin of a few of our reaction products. Lastly, we present PES calculations to suggest chemical mechanisms that may drive the formation of the detected products for the $C_7^{\bullet+}$ dissociation product. All of the identified reactions in this work are summarized in Table 6.1.

Table 6.1: List of the identified (ion-neutral) reactions in this work.

$C_5H^+ + H_2O$	$\longrightarrow$	$C_5OH_3^+$
$C_7^{\bullet+} + H_2O$	$\longrightarrow$	$C_7OH^+ + H^\bullet$
$C_7H^+ + H_2O$	$\longrightarrow$	$C_7OH_3^+$
$C_7OH_3^+$	$\longrightarrow$	$C_6H_3^+ + CO$
$C_9^{\bullet+} + H_2O$	$\longrightarrow$	$C_9OH^+ + H^\bullet$
$C_9H^+ + H_2O$	$\longrightarrow$	$C_9OH_3^+$
$C_9OH_3^+$	$\longrightarrow$	$C_8H_3^+ + CO$
$C_{10}^{\bullet+} + H_2O$	$\longrightarrow$	$C_{10}OH_2^+$
$C_{10}OH_2^+$	$\longrightarrow$	$C_9H_2^+ + CO$
$C_{11}^{\bullet+} + H_2O$	$\longrightarrow$	$C_{11}OH_2^+$

6.3.1 Mass spectra for various V_{RF}

A typical mass spectrum obtained after the electron impact ionization of coronene without applying our SWIFT pulse is shown in Fig. 6.10. The fragmentation product range that is trapped inside the QIT following $\mathbf{Cor}^{\bullet+}$ dissociation can be adjusted by changing V_{RF} and an example of this is shown in Fig. 6.2. The mass spectra over the full mass range are shown in Fig. 6.11. The spectra at different values of V_{RF} show species over different mass ranges because the stability of ions depends on V_{RF} (see eqs. 6.1 and 6.2). In Fig 6.2, m/z 132, 85 and 61 have the highest intensity for a V_{RF} of 2100, 1200 and 850 V, respectively. Interestingly, for V_{RF} = 850 V, peaks are observed at m/z 77, 79 and 95 that are hardly present for V_{RF} = 1200 V, while these masses do fall within the stability range of the ion trap. This is also observed by Sundararajan *et al.* (2024) for the dissociation of corannulene ($C_{20}H_{10}$), albeit at different V_{RF}. Furthermore, earlier works (Panchagnula *et al.* 2024; Hrodmarsson *et al.* 2022, 2023) have shown that bare carbon clusters ($C_n{}^{\bullet+}$ with $n \geq 10$) are formed from PAH dissociation and these species are accompanied by their ^{13}C isotopologues and/or their singly hydrogenated variants. Thus, the appearance of m/z 125 at V_{RF} = 1200 V between m/z 120 ($C_{10}{}^{\bullet+}$) and 132 ($C_{11}{}^{\bullet+}$) is surprising. This observation suggests that gas-phase reactions involving the fragment ions formed by dissociating $\mathbf{Cor}^{\bullet+}$ occur inside the trap.

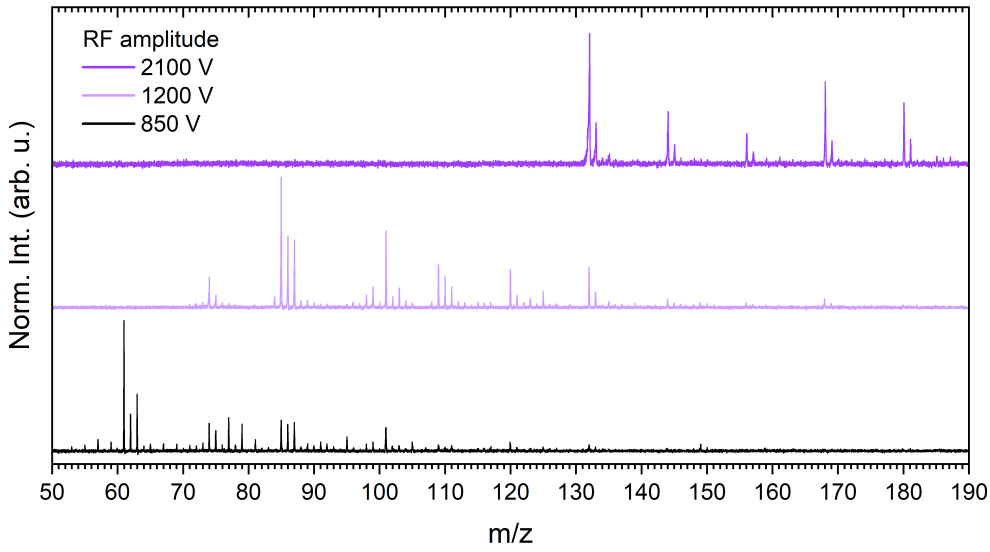

Figure 6.2: Mass spectra following the dissociation of $\mathbf{Cor}^{\bullet+}$ at different V_{RF} in the m/z 50 − 190 range. All spectra are normalized to their most intense peak in the respective mass range. The data recorded at V_{RF} = 2100 and 1200 V are taken from Panchagnula *et al.* (2024)

6.3.2 Chemistry of isolated dissociation fragments

Gas-phase chemical reactions of trapped ions with water in the ion trap are investigated. It must be noted here that the ions are formed inside our room-temperature ion trap through the photodissociation of $\mathbf{Cor}^{\bullet+}$ and are trapped in an RF field. Hence the ions do not have a well-defined kinetic and internal energy when reacting with water.

The reactions are studied by isolating fragment ions in a specific mass range of about 3 amu wide using SWIFT. Unfortunately, this SWIFT range cannot be narrowed down to a

signal of a single amu wide, as this would not result in clean isolation, and moreover, it would also significantly decrease the intensity of the mass signal of interest. This means that the ^{13}C isotopologue and/or singly hydrogenated species, as well as species with one hydrogen less can still be present after filtering the trap with SWIFT and these may also contribute to the subsequent reactions that give rise to the observed products. After isolation using SWIFT, we analyzed the newly formed peaks that show up in the spectra as a result of chemistry involving the isolated ions.

In Fig. 6.3, the mass spectra resulting from $\mathbf{Cor}^{\bullet+}$ dissociation and subsequent isolation of the signals centered at $C_n{}^{\bullet+}$ for $n = 10, 11$ and C_mH^+ for $m = 5, 7, 9$ are presented. In these spectra, we put the ion of interest (the species shown in the label) in the center of the mass spectrum. The other peaks that are potentially chemically related to this signal are presented on a mass difference (Δ m/z) scale with respect to the ion of interest. Bare in mind that the peaks at 1 amu lower and 1 amu higher could also be present in these mass spectra, as this is how we designed our SWIFT pulse (vide supra). However, there is no sign of the bare carbon ions when we isolate the protonated clusters C_9H^+, C_7H^+ and C_5H^+, which either means that these species do not form, or that these species are highly reactive and react away in our trap. We will use our isolation techniques in the next section to show that the latter is in fact true.

The newly formed peaks outside of the isolated mass range in the mass spectra in Fig. 6.3 clearly show that gas-phase reactions occur in the ion trap for all six of the investigated fragment ion ranges. The reactivity of $C_{11}{}^{\bullet+}$ seems significantly less pronounced than those of $C_{10}{}^{\bullet+}$ and the protonated fragments, as the intensities of the product ion signals are larger for the latter species. All fragment ions show products in the Δ m/z +16 to +19 range, that are indicative of a reaction of the $C_n{}^{\bullet+}$ or C_mH^+ and their ^{13}C isotopologues with H_2O, potentially followed by stabilization of the initial adduct, or by H or H_2 loss. Interestingly, the mass spectra resulting from the mass-isolated (closed-shell) protonated species, which by the design of their SWIFT pulses could also include the pure carbonaceous radical cations, exhibit their most pronounced peaks at Δ m/z +16 and +18.

The $C_{10}{}^{\bullet+}$, C_9H^+ and C_7H^+ mass difference spectra show a clear peak at Δ m/z −10. The formation of these ions cannot be explained by a unimolecular reaction of the ions of interest because it would need to lose ten hydrogen atoms. Instead, these species could be formed through the loss of m/z 26 or 28 from the H_2O addition products at Δ m/z +16 or +18, respectively. The first case would require C_2H_2 loss from the Δ m/z +16 product, which is unlikely as the Δ m/z +16 product is of the $C_{10}O^{\bullet+}$ composition for the reaction of $C_{10}{}^{\bullet+}$ and of C_nOH^+ or HC_nO^+ composition for the reactions involving C_9H^+ and C_7H^+. For all these structures the number of hydrogen atoms is insufficient to lose C_2H_2. Hence, it could only be the loss of C_2H_4 or CO. Again, the number of available hydrogen atoms prevents the loss of C_2H_4, so the Δ m/z −10 product can only be formed by CO loss from the Δ m/z +18 reaction product formed by reaction with water. The exact origin of these m/z −10 reaction products formed in the C_7H^+ and C_9H^+ experiments will be investigated in further detail in the next section by sweeping the SWIFT pulse over the isolated mass range.

Minor reaction products at Δ m/z +2 and +4 are seen in the $C_{10}{}^{\bullet+}$, C_7H^+ and C_5H^+ spectra. Moreover, the C_5H^+ spectra also shows peaks at Δ m/z −4 and −6, and some small peaks are seen in the Δ m/z −24 to −11 range of the C_7H^+ spectra. The origin of these minor reaction products is difficult to determine and these species will not be considered in our further analysis.

6.3.3 Identification of the origin of reaction products

To gain further insights into the gas-phase reactions with H_2O inside the ion trap, we investigated the C_7H^+ and C_9H^+ mass regions by stepping the V_{RF} from 1200 to 1300 V and 1450 to 1550 V, respectively, in increments of 10 V. This is done while a SWIFT pulse is active

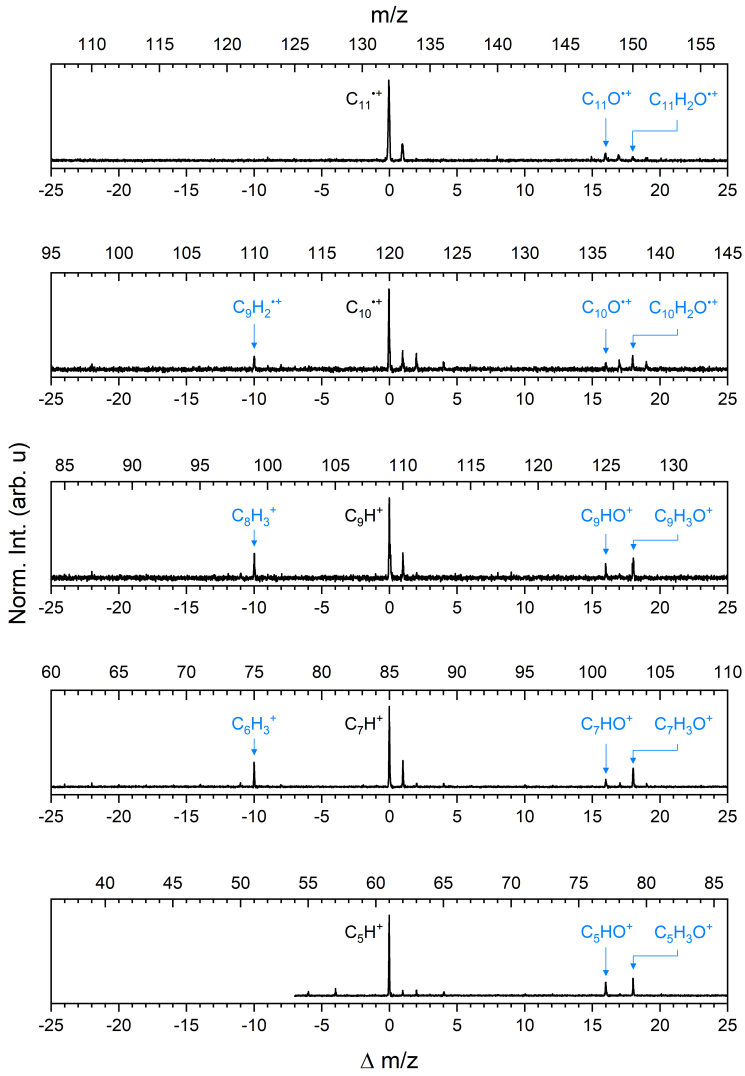

Figure 6.3: Mass difference spectra of $C_n{}^{\bullet+}$ for $n = 10, 11$ and C_mH^+ for $m = 5, 7, 9$. The top of each spectrum represents the absolute mass (m/z). A SWIFT pulse is constructed for each mass, such that it captures a series of masses with Δ $m/z \sim \pm 1$. For C_5H^+, the masses lower than Δ m/z -7 are outside of the stability region of the trap and are hence not detected. The chemical formulas shown in black are the central species of the SWIFT isolated masses and those shown in blue are formulas of the reaction products for Δ m/z -10, $+16$ and $+18$ (see text). All spectra are normalized to the ion of interest.

that expels either the $C_7H_m^+$ for $m = 1 - 3$ or the $C_9H_n^+$ for $n = 1 - 4$ mass ranges at central V_{RF}'s of 1250 and 1500 V, respectively. At the extremes of the V_{RF} ranges (i.e., 1200 and 1300 V for C_7H^+ and 1450 and 1550 V for C_9H^+), no ions in the trap are affected by our SWIFT mass filter and all ions are retained. The resulting mass peaks at each of the V_{RF} settings (11 in total for each series) are integrated and the signals are normalized. The stability factor of the ions, β_z, allows for comparison between V_{RF} and the SWIFT range, as both of these parameters are related to β_z (see eqs. 6.1 – 6.3). First, the regular mass spectra for varying V_{RF} are presented and next the intensities of our ion signals for each m/z value as a function of the β_z value are shown.

6.3.3.1 Reactions in the C_7H^+ mass region

Figure 6.4 shows the mass spectra in the m/z 80 to 105 region for the V_{RF} sweep measurement from 1200 to 1300 V. The mass spectra over the full mass range are shown in Fig. 6.12.

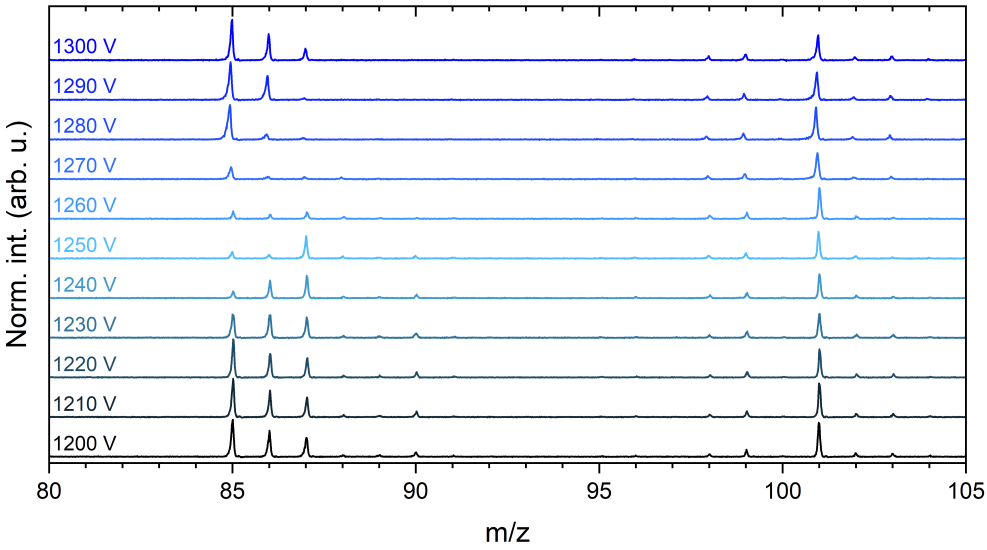

Figure 6.4: Mass spectra for the V_{RF} step measurement from 1200 to 1300 V in the m/z 80 to 105 mass region. The SWIFT region is kept constant, while increasing the V_{RF} by 10 V between each measurement, hence tuning over the stability parameter, β_z. The effect of this can be seen by the disappearing and reappearing peaks between m/z 85 and 90.

The peaks at m/z 85, 86, 87 and 101 are the most intense ones in this measurement. Increasing V_{RF} moves the active SWIFT region toward higher masses. This is clearly seen by the subsequent decrease in intensity for m/z 85, 86 and 87 from $V_{RF} = 1230$ V and increase from $V_{RF} = 1270$ V. The peaks are integrated and normalized at each V_{RF} setting. The resulting normalized integrated intensities as a function of β_z are shown in Fig. 6.5.

It is clear that the SWIFT pulse works as intended, as the signals at m/z 85, 86 and 87 all dip around the same β_z value when the V_{RF} is such that they are within the SWIFT window. Also, a dip in intensity is seen for m/z 101 and 103, which is expected as these were also observed in Fig. 6.3 and attributed to being possible products formed from the reaction of species in the C_7H^+ mass region with water. However, the decrease in intensity for m/z 101 is not as large as for m/z 85, 86 and 87. Possibly, m/z 101 is already substantially formed during the 1 s irradiation and SWIFT phase of the parent ion, i.e., while the cloud is irradiated with the 10 laser pulses. When a SWIFT pulse is applied to the QIT, it does not

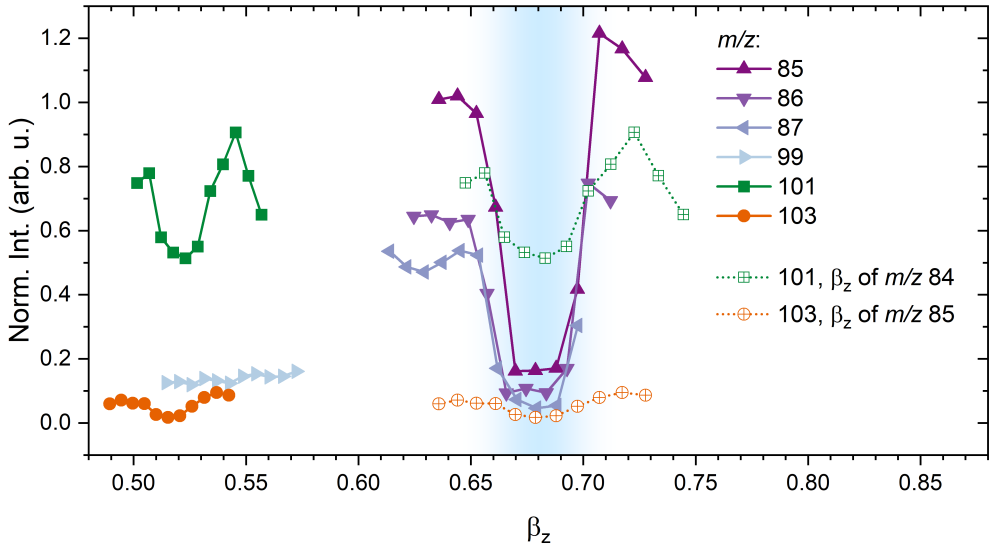

Figure 6.5: Integrated intensities of the m/z 80 to 105 mass region as function of β_z. The region where SWIFT was active is indicated by the blue shaded area. Masses depicted with a dotted line and crossed symbols are plotted with the β_z value of a different mass, which is shown in the legend.

instantly expel ions, but it rather excites their Lissajous trajectories until the ions' motion exceeds the QIT dimensions and is thereby removed and the time this takes varies per m/z (Guan & Marshall 1993). Reactions in the trap may have already taken place in the time required to remove the reactant ions from the trap. In the case that reaction has completed, the resulting ion is no longer affected by the SWIFT pulse and is therefore retained in the trap and measured in the TOF mass spectrum. Another explanation could be that not all of m/z 101 is the result of a reaction. However, Sundararajan *et al.* (2024) shows the total disappearance of m/z 101 for the dissociation of sumanene when the C_7H^+ region is not stable in the trap, indicating that the latter explanation is not likely.

The primary reactant that forms m/z 101 and 103 ions can now be determined. To this end, the normalized intensity of our product ion is plotted as a function of β_z values corresponding to different masses until the dip matches with the active SWIFT region (see Fig. 6.14 and 6.15 for the full analysis), and when the two dips in the mass signals match in the β_z domain, it has been established that the two species are chemically connected. The integrated intensities of the m/z 101 and 103 signals are shown in Fig. 6.5, but they are plotted using the β_z parameters of m/z 84 and 85, respectively, which result in the best match of the depletion of the ion signal. This means that m/z 101 and 103 (partly) originate from the reaction of m/z 84 ($C_7^{\bullet+}$) and 85 (C_7H^+) with water, respectively. Because, the difference between m/z 101 and 84 is m/z 17, this product is formed by the addition of water followed by the loss of a hydrogen atom, which removes excess energy from the system. The m/z 103 product is a direct addition product, which is likely stabilized through one or two processes: stabilization through collisions with the helium buffer gas in the trap and/or radiative cooling. Another mechanism proceeds via the loss of a CO molecule, resulting in the formation of the $C_6H_3^+$ ion, as seen in Fig. 6.3.

Interestingly, we only observe a tiny $C_7^{\bullet+}$ peak at m/z 84 for $V_{\mathrm{RF}} = 1200$ V in Fig. 6.2. However, no Δ m/z -1 peak (corresponding to the pure $C_7^{\bullet+}$ signal at m/z 84) is seen in Fig. 6.3 for the C_7H^+ mass spectrum. Moreover, Fig. 6.4 has no indication of a peak at

m/z 84 either. This suggests that the signal is very sensitive to the amount of water present in the trap and the reaction of $C_7^{\bullet+}$ with H_2O (almost completely) depletes the $C_7^{\bullet+}$ fragment that originates from $\mathbf{Cor}^{\bullet+}$ photodissociation.

6.3.3.2 Reactions in the C_9H^+ mass region

Figure 6.6 shows the mass spectra in the m/z 105 to 130 mass region for the V_{RF} step measurement from 1450 to 1550 V. The mass spectra over the full mass range are shown in Fig. 6.13.

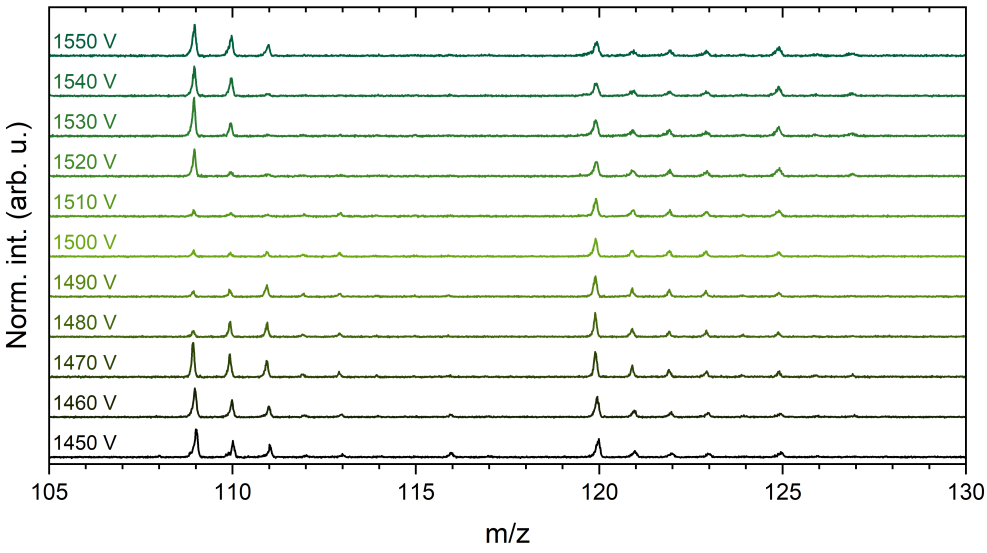

Figure 6.6: Mass spectra for the V_{RF} sweep measurement from 1450 to 1550 V in the m/z 105 to 130 mass region. The SWIFT region is kept constant, while increasing the V_{RF} by 10 V between each measurement, hence tuning over the stability parameter, β_z. The effect of this can be seen by the disappearing and reappearing peaks between m/z 109 and 113.

The species at m/z 109, 110, 111 and 120 exhibit the most intense signals in this measurement. Interestingly, the intensity of m/z 125 is significantly lower, compared to m/z 101 in Fig. 6.4. This could indicate that the reactivity of the species in the C_9H^+ mass region is less compared to C_7H^+, or that H_2O was more abundant in the C_7H^+ measurement. Similar to the C_7H^+ measurement, a change in the intensity for m/z 109, 110 and 111 is seen when tuning V_{RF} from 1480 to 1520 V, as the active SWIFT region moves toward higher masses with increasing V_{RF}. The mass peaks are integrated and the integrated intensities are normalized at each V_{RF} setting. The resulting normalized integrated intensities as a function of β_z are shown in Fig. 6.7.

Similar to the C_7H^+ mass region, we see a dip in intensity for m/z 109, 110, 111 and 112 when the β_z values of these ions fall within the SWIFT region. Again, this is accompanied by a dip in intensity for m/z 125 and 127, as one would expect based on the mass spectra in Fig. 6.3. The intensity decrease for m/z 125 is less pronounced compared to that of m/z 109, 110 and 111, which was also observed in the C_7H^+ measurement.

The normalized intensity of m/z 125 and 127 with β_z values of different masses are investigated to match their dip with the active SWIFT region and these are shown in Fig. 6.16 and 6.17. In Fig. 6.7, only the plots for the β_z values that provide the best match are shown. This figure shows that m/z 125 and 127 (partially) find their origin in the reaction of m/z 108

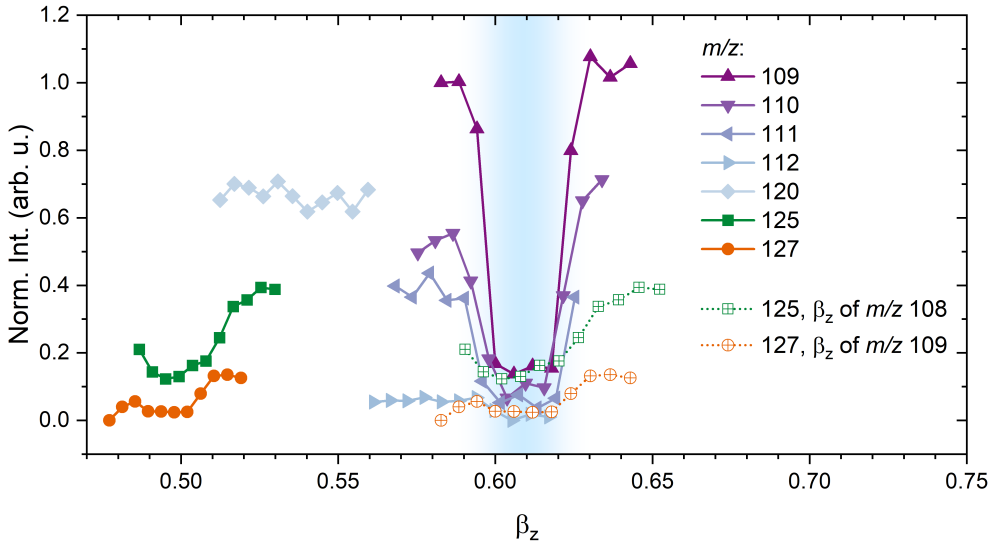

Figure 6.7: Integrated intensities of the m/z 105 to 130 mass region as function of β_z. The region where SWIFT was active is indicated by the blue shaded area. Masses depicted with a dotted line and crossed symbols are plotted with the β_z value of a different mass, which is shown in the legend.

($C_9^{\bullet+}$) and 109 (C_9H^+), respectively, with water. Again, we only observe a very small signal at m/z 108 for V_{RF} = 1200 V in Fig. 6.2, no Δ m/z −1 peak (corresponding to $C_9^{\bullet+}$) in Fig. 6.3 for the C_9H^+ region and Fig. 6.6 has no indication of a $C_9^{\bullet+}$ peak at m/z 108 either. Similarly to the case for $C_7^{\bullet+}$, the reaction of $C_9^{\bullet+}$ with H_2O (almost completely) depletes the $C_9^{\bullet+}$ fragment signal. The dissipation of excess energy in the product ions may proceed through the same mechanisms as described for the $C_7^{\bullet+}$ and C_7H^+ reactions.

6.3.4 Effect of geometry on reactivity

We now compare the reactivities of the various ions of different masses to investigate the effect of their structure on their reactivity. As mentioned earlier, low mass carbocations were found to be formed as linear species and cyclic species, while the larger ions only form as cyclic structures and these may exhibit differences in reactivity. From Fig. 6.3, one can clearly see that the reactivity of $C_{11}^{\bullet+}$ toward gas-phase water appears to be less compared to the other investigated ions, as the intensities of the reaction products in the Δ m/z +16 to +19 range are much lower. Furthermore, the $C_{11}^{\bullet+}$ measurements lack a clear Δ m/z −10 peak that would correspond to the subsequent CO loss from the adduct, thus giving hints about the differences in the reactivity of the species.

Interestingly, the $C_{10}^{\bullet+}$ and $C_{11}^{\bullet+}$ measurements show four product ion peaks in the Δ m/z +16 to +19 range compared to only two clear product peaks for the C_5H^+, C_7H^+ and C_9H^+ measurements. From the reactant identification in Fig. 6.5 and 6.7 it was determined that $C_7^{\bullet+}$ and $C_9^{\bullet+}$ play important roles in the formation of products, despite not being directly observed in Fig. 6.3. Therefore, the C_7H^+ and C_9H^+ measurements in Fig. 6.3 likely contain species formed by reactions with both $C_n^{\bullet+}$ and C_mH^+. The width of our SWIFT pulse allowed Δ m/z ±1 to be visible in the spectra as well, so the previous also holds true for the $C_{10}^{\bullet+}$ and $C_{11}^{\bullet+}$ measurements. Because these measurements all have $C_n^{\bullet+}$ and C_mH^+ as possible reactants, the difference between the product signals found in the Δ m/z +16 to

+19 range cannot be explained by the available reactants but must have a different origin.

The difference in reactivity can be further investigated by exploring the possible geometries of the reactants. Von Helden and co-workers (von Helden *et al.* 1993; von Helden *et al.* 1993a,b, 1994; Lee *et al.* 1997) studied the geometry of carbon cluster ions and protonated carbon clusters formed by the excimer laser ablation of a carbon rod using ion mobility measurements. They found $C_n{}^{\bullet+}$ clusters for $n = 11 - 20$ to be entirely monocyclic, while for $n = 7 - 10$ the species exist in both a monocyclic and linear geometry. The species with $n = 3 - 6$ were all found to be linear. Moreover, the $C_{10}{}^{\bullet+}$ cluster is found to have between 85 and 100% of its isomers to be of monocyclic geometry, while for $C_8{}^{\bullet+}$ and $C_9{}^{\bullet+}$ this percentage drops to 18-35% being monocyclic. Interestingly, the contribution of cyclic $C_7{}^{\bullet+}$ clusters varies significantly depending on the experimental conditions used for its formation between 32 and 82%. The protonated carbon clusters were also found to have either monocyclic or linear geometries. The species $C_{11}H^+$ and $C_{10}H^+$ are mainly cyclic and were found make up about 86 and 68% to the total signal, respectively. This changes with C_9H^+ where the cyclic isomer contribution is only about 4%. Von Helden and co-workers did not consider smaller protonated carbon clusters, however, if one considers the trend from the pure carbon clusters then the C_mH^+ for $m \leq 9$ are highly likely to be of linear geometry.

These works show that $C_{10}{}^{\bullet+}$ is a species in a transitioning phase from monocyclic to linear, possibly explaining why the $C_{10}{}^{\bullet+}$ mass difference spectra show components of both the $C_{11}{}^{\bullet+}$-type reactivity and the smaller protonated fragments' reactivity. Potentially, the four peaks in the Δ m/z +16 to +19 region are indicative of products formed from reactions of the monocyclic geometry as they are only present for $C_{10}{}^{\bullet+}$ and $C_{11}{}^{\bullet+}$ and partly present for $C_7{}^{\bullet+}$, as was seen in the C_7H^+ measurement. With that same reasoning, the Δ m/z −10 peak could be indicative of a reaction involving a linear geometry, as it is only clearly present for the species that contain a significant contribution of linear isomers. However, one should be careful comparing the Δ m/z −10 peaks, as the Δ m/z −10 component of $C_{10}{}^{\bullet+}$ signifies a different species than the Δ m/z −10 with respect to the mass of the *protonated* species C_7H^+ and C_9H^+. If we were to overlap them in a mass difference plot based on the pure carbon cluster ion, i.e., $C_7{}^{\bullet+}$ and $C_9{}^{\bullet+}$, the Δ m/z −10 peak would shift to Δ m/z −9 for $C_7{}^{\bullet+}$ and $C_9{}^{\bullet+}$, thus indicating that different reaction mechanisms are at play. Nevertheless, this could still hint toward a varying geometry between the reactants being a potential underlying cause of the difference in their reactivity.

6.3.5 Comparison to previous works on reactivity of $C_n{}^{\bullet+}$ and C_mH^+

Our measurements can be compared to studies done by McElvany and co-workers (McElvany *et al.* 1987; McElvany 1988; Parent & McElvany 1989) on the reactivity of pure $C_n{}^{\bullet+}$ with $n = 3 - 9$ carbon cluster cations with C_2H_2, C_2H_4, HCN and D_2. They found that reactions with C_2H_2, C_2H_4 and D_2 favor the addition of the neutral to the ionic species, followed by the elimination of a hydrogen (or deuterium) atom. The reaction with HCN shows a similar preference, however, this only holds for $n = 3 - 5, 7$. Our findings of $C_7{}^{\bullet+}$ and $C_9{}^{\bullet+}$ reacting with H_2O thus match the behavior of pure carbon cluster cations reacting with other closed-shell species.

The reaction of C_mH^+ for $m = 3 - 9$ with C_2H_2 and HCN has also been studied by McElvany and co-workers (McElvany 1988; Parent & McElvany 1989). For the reaction with C_2H_2, it was observed that the process involves the addition of the neutral C_2H_2 onto the ion, followed by the loss of a hydrogen atom for $m = 5, 6, 8$, whereas no hydrogen atom is lost for $m = 7, 9$. The reaction with HCN proceeds via addition followed by hydrogen elimination for $m = 4, 6$, but no hydrogen is lost for $m = 3, 5, 7$. This is similar to what we found for C_7H^+ and C_9H^+. Interestingly, for the reaction with C_2H_2, C_5H^+ loses a hydrogen atom, however Fig. 6.3 does not show a clear hydrogen loss peak at Δ m/z +17. Thus, indicating

that the reaction of C_5H^+ with H_2O prefers to lose no hydrogen atoms, similar to C_7H^+ and C_9H^+.

Raksit & Bohme (1983) studied the reaction of C_3H^+ with H_2O and other neutral reactants in a selected-ion flow tube reactor. Although this reactant ion is outside our investigated mass range, it can still provide general insights into the reactivity. The main reaction product of C_3H^+ with H_2O was found to be $HCO^+ + C_2H_2$. For C_7H^+, the resulting products would be analogous to $HC_5O^+ + C_2H_2$, which if present would have been found at Δ m/z −8 in Fig. 6.3. Likely, this reaction is only possible for C_3H^+ due to its small size allowing specific isomerizations that lead to C_2H_2 loss. The second possible reaction pathway of C_3H^+ with H_2O was found to result in $C_2H_3^+ + CO$, which we also observe for C_7H^+ and C_9H^+. Another reaction led to the formation of $HC_3O^+ + H_2$, which seems to happen for our C_5H^+, C_7H^+ and C_9H^+ reactants as well, because both Δ m/z +16 and +18 are observed for those ions in Fig. 6.3. Unfortunately, our study does not allow for the determination of branching ratios and the assignment of the signal at Δ m/z +16 as being partly formed through the loss of H_2 from Δ m/z +18 is only tentative.

6.3.6 Potential energy surface of the $C_7^{\bullet+} + H_2O$ reaction

With the likely geometries of the **Cor**$^{\bullet+}$ dissociation fragments in mind, a PES of the reactions can be constructed to investigate the high reactivity observed in the experiments. Here, we only considered the $C_7^{\bullet+} + H_2O$ reaction, but the mechanism is expected to be very similar for the reaction involving $C_9^{\bullet+}$. A PES is generated for both the linear (l-$C_7^{\bullet+}$) and cyclic (c-$C_7^{\bullet+}$) geometries as both of these may exist in our trap (von Helden *et al.* 1993a,b). The final product at m/z 101 may comprise many different isomers. We investigated the two lowest energy isomers of m/z 101, HC_7O^+ and C_7OH^+, for the l-$C_7^{\bullet+} + H_2O$ reaction and linear and cyclic HC_7O^+ for the c-$C_7^{\bullet+} + H_2O$ reaction.

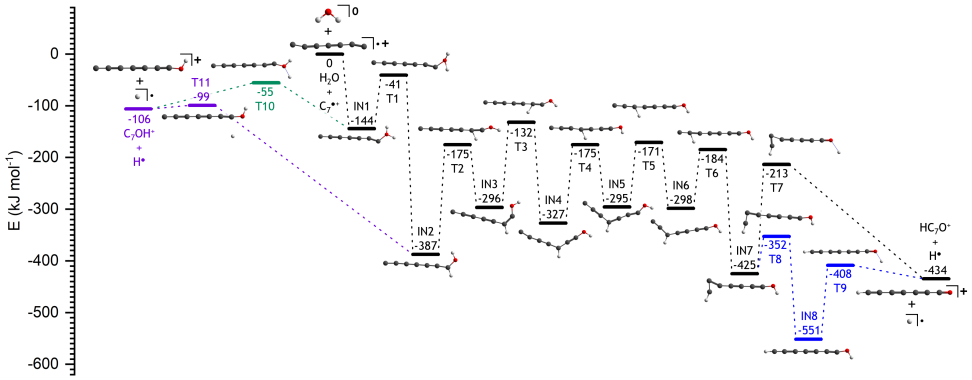

Figure 6.8: Potential energy surface of the l-$C_7^{\bullet+} + H_2O$ reaction calculated using B3LYP/6-311++G(d,p), resulting in $HC_7O^+ + H^\bullet$ (black and blue) and $C_7OH^+ + H^\bullet$ (green and purple).

A PES of the l-$C_7^{\bullet+} + H_2O$ reaction is shown in Fig. 6.8, resulting in the product channels $HC_7O^+ + H^\bullet$ and $C_7OH^+ + H^\bullet$. Interestingly, the calculated l-$C_7^{\bullet+}$ geometry is not fully linear but has its outer carbon atoms under an angle, pointing in opposite directions. The isomer where the outer carbon atoms point in the same direction is also found and has a very similar energy. The first thing to note about the PES, is that the initial addition is barrierless and all transition states are submerged, which compliments the high reactivity of the $C_7^{\bullet+}$ ion in our experiments. The H_2O molecule prefers to bind to one of the outer carbon atoms

of *l*-$C_7^{\bullet+}$, creating **IN1** at −144 kJ mol^{-1}. A hydrogen atom from the H_2O moiety can migrate to the carbon chain through **T1** at −41 kJ mol^{-1}. This step also happens to be the rate-limiting transition state for the formation of HC_7O^+. Instead of migration, a hydrogen atom can also be lost from the H_2O moiety through **T10** at −55 kJ mol^{-1}, immediately resulting in $C_7OH^+ + H^\bullet$ at −106 kJ mol^{-1}. From **T1**, **IN2** is formed, where a hydrogen atom is bound to the carbon atom adjacent to the OH group. This intermediate state has an energy of −387 kJ mol^{-1}. The hydrogen atom bound to carbon can be lost through **T11** at −99 kJ mol^{-1}, thus forming $C_7OH^+ + H^\bullet$. This same hydrogen can also migrate over the carbon chain toward the bare end through **T2-T6**, of which the highest energetic step is **T3** at −132 kJ mol^{-1}. In principle, one of the two hydrogen atoms can be lost from any of the species encountered along the PES, potentially forming a multitude of *m/z* 101 isomers that differ in the position of the remaining hydrogen atom. Interestingly, the hydrogen migration of **T6** leads to the formation of a three-membered ring in **IN7**, which has an energy of −425 kJ mol^{-1}. Opening of this ring through **T8** at −352 kJ mol^{-1} results in **IN8** at −551 kJ mol^{-1}, where the molecule has adopted a linear geometry again with the hydrogen atoms at either end. Losing the hydrogen from the oxygen via **T9** at −408 kJ mol^{-1}, results in $HC_7O^+ + H^\bullet$ at −434 kJ mol^{-1}. When the hydrogen is removed from the oxygen atom of **IN7**, through **T7** at −213 kJ mol^{-1}, the ring opens simultaneously, thus forming $HC_7O^+ + H^\bullet$.

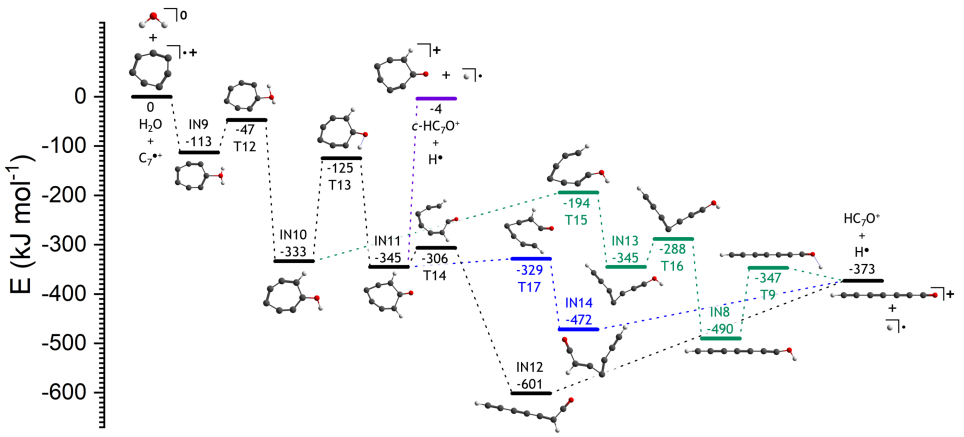

Figure 6.9: Potential energy surface of the *c*-$C_7^{\bullet+}$ + H_2O reaction calculated using B3LYP/6-311++G(d,p), resulting in $HC_7O^+ + H^\bullet$ (black, blue and green) and *c*-$HC_7O^+ + H^\bullet$ (purple).

Figure 6.9 shows a potential mechanism for the *c*-$C_7^{\bullet+}$ + H_2O reaction, resulting in linear and cyclic $HC_7O^+ + H^\bullet$. The H_2O molecule can attack *c*-$C_7^{\bullet+}$ on any of the carbons and form **IN9** at −113 kJ mol^{-1}. Also for the reaction of this cyclic species, we note that the initial association is barrierless and all transition states are submerged. Upon forming the initial adduct, a hydrogen atom can migrate to the closest available carbon atom through **T12** at −47 kJ mol^{-1} to form **IN10** with an energy of −333 kJ mol^{-1}. Opening the ring between the CH and COH groups via **T15** at −194 kJ mol^{-1} leads to **IN13** at −345 kJ mol^{-1}, which contains a three-membered ring in the center of the molecule. Opening the three-membered ring over **T16** at −288 kJ mol^{-1} leads to the formation of $HC_7O^+ + H^\bullet$ at −373 kJ mol^{-1} via **IN8** and **T9**, as already shown in Fig. 6.8. A hydrogen atom can also be removed from the CH group instead of the OH group, but this would result in a product that is higher in energy by 328 kJ/mol (Fig. 6.8).

Instead of ring opening from **IN10**, hydrogen migration can occur through **T13** at −125 kJ mol^{-1}, where the hydrogen from the OH group moves to the nearest bare carbon, forming **IN11** at −345 kJ mol^{-1}. Either of the two hydrogen atoms can be removed from **IN11** without a reverse barrier, resulting in c-HC_7O^+ + $H^\bullet$ at −4 kJ mol^{-1}. Opening the ring of **IN11** on either side of the CO moiety results in **IN12** at −601 kJ mol^{-1} or **IN14** at −472 kJ mol^{-1}, via **T14** at −306 kJ mol^{-1} or **T17** at −329 kJ mol^{-1}, respectively. **IN12** presents a linear structure while **IN14** contains a three-membered ring. Removing the hydrogen atom closest to the CO group of **IN12** results in HC_7O^+ + $H^\bullet$. When **IN14** loses that same hydrogen, the three-membered ring opens simultaneously, forming HC_7O^+ + $H^\bullet$.

On both the linear and cyclic surfaces, the $C_7{}^{\bullet+}$ + H_2O product could stabilize in one of the wells. However, the C_7H^+ region in Fig. 6.3 does not show a high intensity peak for $H_2C_7O^{\bullet+}$/$C_7OH_2{}^{\bullet+}$ (m/z 102), while it does for HC_7O^+/C_7OH^+ (m/z 101). Hence, experimentally, it is shown that the $C_7{}^{\bullet+}$ + H_2O reaction prefers to proceed via the loss of a single hydrogen atom. Furthermore, because the transition states on both the l-$C_7{}^{\bullet+}$ + H_2O and c-$C_7{}^{\bullet+}$ + H_2O PES are all submerged with respect to the entrance channel, the reaction can proceed regardless of the geometry (linear or cyclic) of $C_7{}^{\bullet+}$, even in low-temperature interstellar environments.

Much like the $C_7{}^{\bullet+}$ reaction described above, the $C_9{}^{\bullet+}$ reaction can occur in both its linear and cyclic geometry (von Helden *et al.* 1994) and exhibits similar reactivity as $C_7{}^{\bullet+}$ (McElvany *et al.* 1987; McElvany 1988; Parent & McElvany 1989). Arguably, if the PES for the l-$C_9{}^{\bullet+}$ + H_2O and c-$C_9{}^{\bullet+}$ + H_2O reactions would be constructed, it could be analogous to the $C_7{}^{\bullet+}$ PES shown in Fig. 6.8 and 6.9.

6.4 Conclusions and astrophysical implications

In this work, the reactivity of **Cor**$^{\bullet+}$ dissociation fragments in a room-temperature ion trap was investigated. To this end, mass ranges of 3 amu wide around the $C_n{}^{\bullet+}$ for $n = 10 - 11$ and C_mH^+ for $m = 5, 7, 9$ ions were isolated and reacted with gas-phase water. Fragments in all ranges are found to react with water and some reactions are followed by the loss of atomic hydrogen from the initial adduct, giving rise to mass peaks at the Δ m/z +16 to +19 range. The species $C_{10}{}^{\bullet+}$, C_9H^+ and C_7H^+ also showed a clear peak at Δ m/z −10 that is shown to form through the addition of water followed by the loss of CO. Diving further into the reactions of C_9H^+ and C_7H^+ using a resonant ejection technique, we find that C_9H^+, $C_9{}^{\bullet+}$, C_7H^+ and $C_7{}^{\bullet+}$ react with water. The reactions of the protonated species give rise to the Δ m/z +18 peak ($C_9OH_3{}^+$ and $C_7OH_3{}^+$). The bare $C_9{}^{\bullet+}$ and $C_7{}^{\bullet+}$ carbon species form the Δ m/z +16 peak (HC_9O^+ and HC_7O^+) that results from a reaction with water followed by the loss of atomic hydrogen. All identified reactions are summarized in Table 6.1.

The reactants, C_9H^+, $C_9{}^{\bullet+}$, C_7H^+ and $C_7{}^{\bullet+}$, are likely direct dissociation fragments from **Cor**$^{\bullet+}$, while their Δ m/z +16 to +19 and Δ m/z −10 species form by subsequent reactions with gas-phase water. Hence, we underscore the conclusion drawn earlier that the low-mass bare carbon species, $C_n{}^{\bullet+}$, with $n = 10 - 15$ form upon PAH cation dissociation (Panchagnula *et al.* 2024; Hrodmarsson *et al.* 2022, 2023). Moreover, we also show indirect evidence that $C_9{}^{\bullet+}$ and $C_7{}^{\bullet+}$ are formed, but these are not observed in the mass spectra due to their high reactivity. These results also highlight the importance of characterizing secondary reactions taking place inside an ion trap in order to correctly assign the direct photodissociation fragments of PAH cations.

The differences in the reactivity of **Cor**$^{\bullet+}$ dissociation fragments was also studied and it was found that this may be linked to the molecular geometry of the formed ions. The $C_{11}{}^{\bullet+}$ species is found to be likely of cyclic geometry, and C_9H^+, $C_9{}^{\bullet+}$ and C_7H^+ are of linear geometry. Potentially, $C_{10}{}^{\bullet+}$ is a species in a transitioning phase from monocyclic to linear and $C_7{}^{\bullet+}$ is produced in both linear and cyclic geometry (von Helden *et al.* 1993; von

Helden *et al.* 1993a,b, 1994; Lee *et al.* 1997). Reactions are found to proceed in a fashion similar to that of previous studies on carbon cluster reactivity conducted in the past. The investigated reaction pathways for the reaction of $C_7^{\bullet+}$ with water resulting in HC_7O^+ and C_7OH^+ support the experimentally observed reactivity of $C_7^{\bullet+}$.

According to the GrandPAH hypothesis (Andrews *et al.* 2015), large (>50 carbon atoms) PAHs are dominant in photon-dominated regions in the ISM. This implies that smaller less stable PAHs are transformed by photodissociation into other carbonaceous species. Many studies on the dissociation of (smaller) PAHs have been conducted (Panchagnula *et al.* 2024; Hrodmarsson *et al.* 2022, 2023; Sundararajan *et al.* 2024; Bouwman *et al.* 2016; de Haas *et al.* 2017; Schleier *et al.* 2024a; Ekern *et al.* 1998; Panchagnula *et al.* 2020; Jochims *et al.* 1994; West *et al.* 2012, 2014a,b, 2018, 2019; Castellanos, P. *et al.* 2018; Zhen *et al.* 2014a), of which some show the appearance of common fragmentation products for PAHs of very different shapes and sizes. These ionic photodissociation fragments of (small) PAHs enrich the ISM.

Due to the low densities in the ISM, chemistry is largely driven by ion-neutral reactions due to their high bimolecular reaction rates caused by strong long-range interactions. In this work, we establish that the reaction of $C_7^{\bullet+}$ – formed through the dissociation of $\mathbf{Cor}^{\bullet+}$ in the ion trap – with water proceeds without a reverse barrier. The product stabilizes by the loss of a hydrogen atom, suggesting that this reaction may occur in the ISM. Therefore, the subsequent reaction of PAH photodissociation fragment ions may be highly relevant for the chemical evolution of the ISM.

Acknowledgements

Harold had a profound impact on the lives of many people, including scientists across the globe and across the various disciplines he worked in. He was the driving force in the field of laboratory astrochemistry, and his passion for research and his mentoring skills inspired countless colleagues and students. We will always treasure his invaluable advice, and his wisdom and thoughtfulness will remain in our hearts.

This material is based upon work supported by the National Science Foundation under Grant No. 2308045. This work was supported in part by NASA's Solar System Exploration Research Virtual Institute (SSERVI): Institute for Modeling Plasma, Atmosphere, and Cosmic Dust (IMPACT). Quantum chemical calculations were carried out on the Dutch national e-infrastructure with the support of SURF Cooperative (EINF-10587).

6.A Appendices

These appendices contain further information to chapter 6. First, we present a typical mass spectrum of coronene after electron impact ionization. Next, we describe the experimental parameters used to collect our data. We continue by showing the mass spectra shown in Fig. 6.2, 6.4 and 6.6 over the full mass range. Lastly, we show the plots of normalized intensities of our ion signals as a function of β_z that help to chemically connect reactants and product ions in the trap.

6.A.1 Coronene electron impact ionization mass spectrum

Fig. 6.10 shows a typical mass spectrum that is obtained upon 70 eV electron impact ionization of neutral coronene, without irradiation the ion cloud and without using our SWIFT mass filtering. Several peaks can be observed in the spectrum, most prominently the coronene cation together with its ^{13}C components as well as up to six hydrogen loss peaks. The coronene dication and C_2H_{2-4} loss peaks are observed as well.

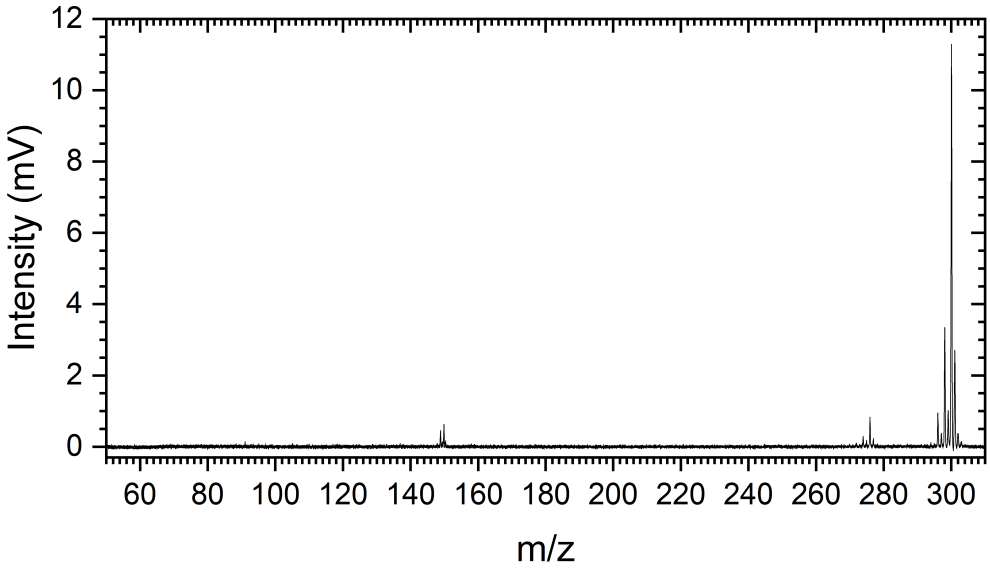

Figure 6.10: A typical mass spectrum obtained after the electron impact ionization of neutral coronene.

6.A.2 Experimental parameters

In this work we present the results from different measurements done at various settings. The V_{RF}, the laser energy used for irradiation and the SWIFT frequency range used for isolation or extraction are listed for each of our measurement series in table 6.2.

Table 6.2: Experimental parameters used in the various measurements throughout this work.

Measurement		V_{RF}	Laser energy	SWIFT range
Fig. #	Description	($\mathrm{V_{pk-pk}}$)	(mJ/pulse)	(Hz)
6.2	2100 V_{RF}	2100	1.1	-
	1200 V_{RF}	1200	2.4	-
	850 V_{RF}	850	4.5	-
6.3	$C_{11}{}^{\bullet+}$	1200	5.0	164331 – 179331
	$C_{10}{}^{\bullet+}$	1100	4.7	166728 – 179228
	C_9H^+	1100	5.0	186662 – 202662
	C_7H^+	900	4.2	198484 – 220484
	C_5H^+	850	4.6	255195 – 305000
6.4 & 6.5	-	1200 → 1300	4.5	299149 – 301149
6.6 & 6.7	-	1450 → 1550	4.9	273767 – 274767

6.A.3 Mass spectra over the full m/z 50 to 310 range

In Fig. 6.11, 6.12 and 6.13 the mass spectra from Fig. 6.2, 6.4 and 6.6, respectively, are shown over the full mass range (m/z 50 to 310).

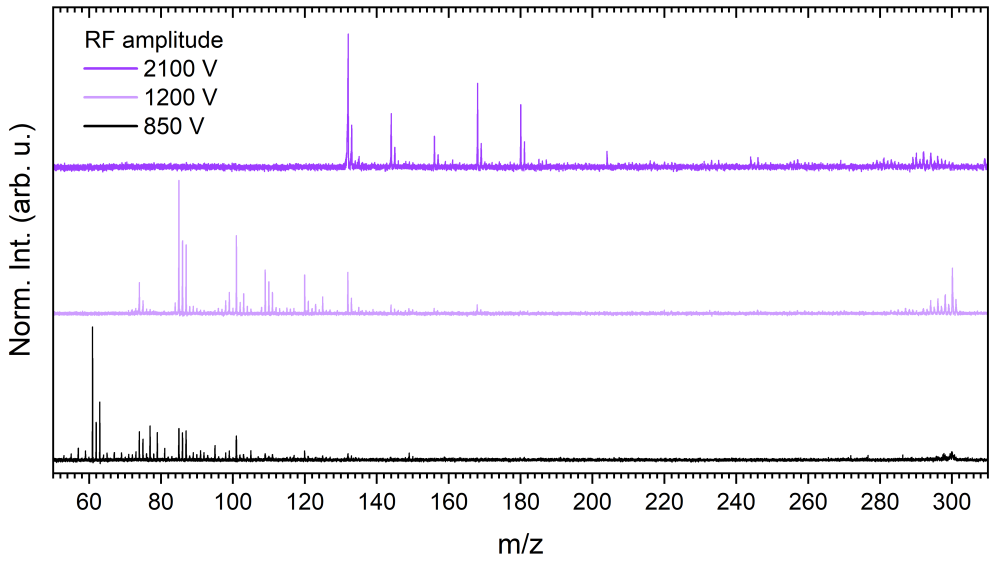

Figure 6.11: Mass spectra following the dissociation of $\mathbf{Cor}^{\bullet+}$ at different V_{RF} in the m/z 50 – 310 range. All spectra are normalized to their most intense peak in the respective mass range. The data recorded at $V_{\mathrm{RF}} = 2100$ and 1200 V are taken from Panchagnula *et al.* (2024)

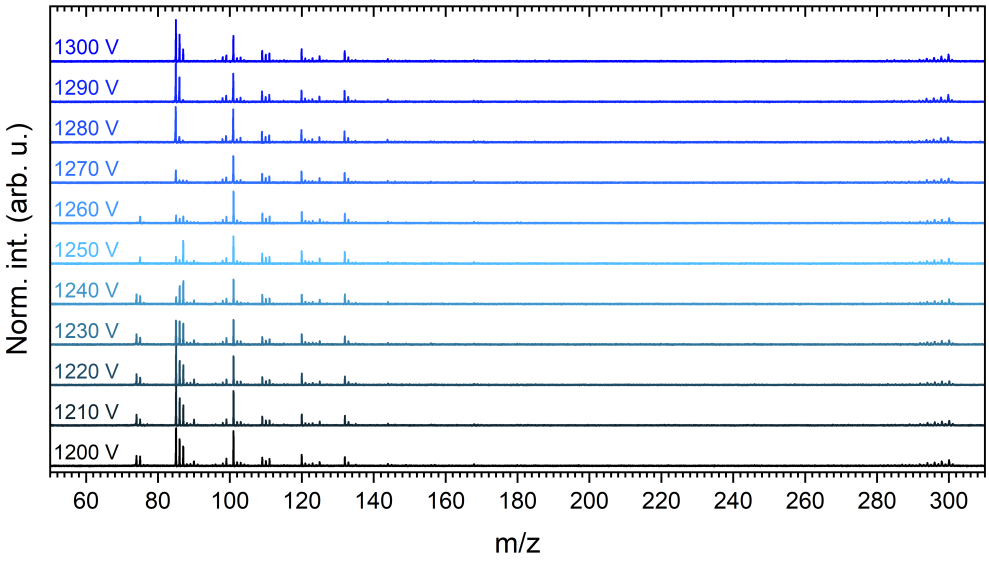

Figure 6.12: Mass spectra recorded for the V_{RF} step measurement from 1200 to 1300 V in the m/z 50 to 310 region. The SWIFT region is kept constant, while increasing the V_{RF} for each measurement, hence tuning over the stability parameter, β_z. The effect of this can be seen by the disappearing and reappearing peaks between m/z 85 and 90.

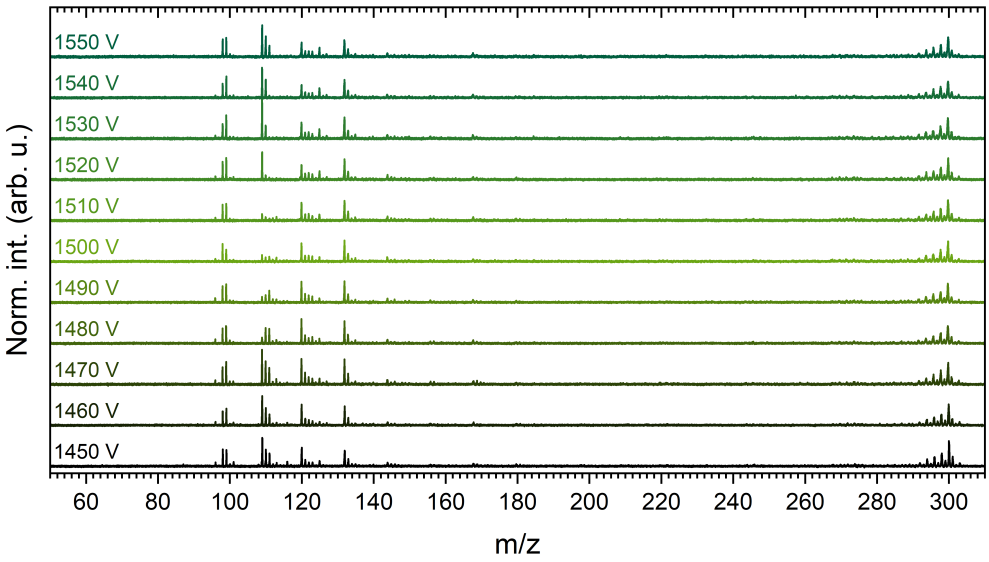

Figure 6.13: Mass spectra recorded for the V_{RF} step measurement from 1450 to 1550 V in the m/z 50 to 310 region. The SWIFT region is kept constant, while increasing the V_{RF} each measurement, hence tuning over the stability parameter, β_z. The effect of this can be seen by the disappearing and reappearing peaks between m/z 109 and 113.

6.A.4 Plotted intensity as function of β_z, for different β_z values

6.A.4.1 The C_7H^+ mass region

Here, the normalized integrated intensities of ion signals are presented as function of β_z for the V_{RF} step measurement (from 1200 to 1300 V) of the C_7H^+ mass region. Fig. 6.14 shows the m/z 101 signal as a function of the different β_z values and Fig. 6.15 shows m/z 103 as a function of the different β_z values.

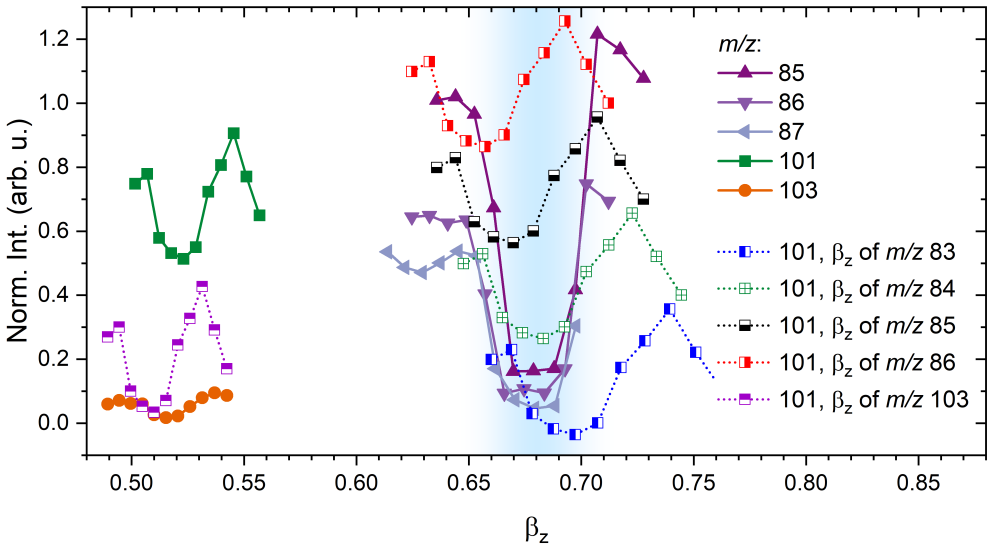

Figure 6.14: Integrated intensities of the C_7H^+ region as function of β_z. m/z 101 is plotted for different values of β_z (dotted line and half-filled square symbols), many of which are not presented in the main manuscript. The region where SWIFT was active is indicated by the blue shaded area. The data presented with the dotted lines is given a vertical offset to improve visibility and facilitate comparison.

From Fig. 6.14 it can be seen that only plotting the m/z 101 signal as a function of the β_z value for m/z 84 makes the dip in signal match with the active SWIFT region. For a β_z of m/z 83, which would correspond to an unrealistic species (i.e. $C_6H_{11}{}^+$), m/z 101 dips at too high of a β_z and for m/z 85 and 86, the signal dips at too low of a β_z. One could argue that the initial dip matches well with m/z 85, however the intensity increase is centered in the active SWIFT region makes this a poor match. The m/z 101 is plotted with the β_z value of m/z 101 as well to make sure that the signal at 101 is not formed from that at 103. The m/z 101 dips and rises too early to be formed from m/z 103. Thus, m/z 101 matches the SWIFT region best when plotted with the β_z of m/z 84.

In Fig. 6.15 we find that the β_z value for m/z 85 makes the m/z 103 signal match the SWIFT region. For a β_z of m/z 83 and 84, m/z 103 dips too late and for m/z 86, m/z 103 dips too early. The signal at m/z 103 is plotted with the β_z value of m/z 101 to investigate a potential link between the two species. From this, it is found that m/z 103 dips and rises too late to have a significant link with m/z 101.

6.A.4.2 The C_9H^+ mass region

The normalized integrated intensity as function of β_z for the V_{RF} step measurement (from 1450 to 1550 V) of the C_9H^+ mass region are presented here. Fig. 6.16 shows the m/z 125

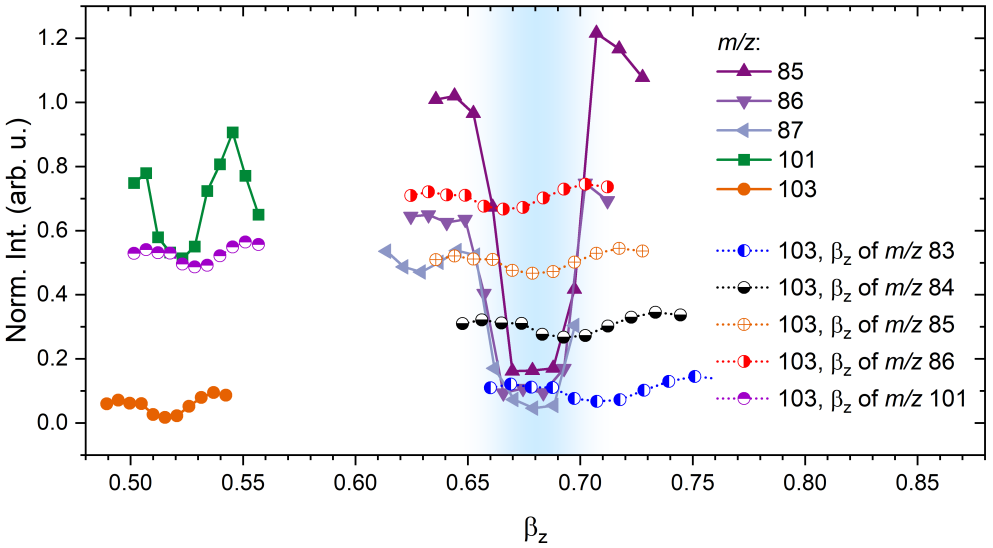

Figure 6.15: Integrated intensities of the C_7H^+ region as function of β_z. m/z 103 is plotted for different values of β_z (dotted line and half-filled circle symbols), many of which are not presented in the main manuscript. The region where SWIFT was active is indicated by the blue shaded area. The data presented with the dotted lines is given a vertical offset to improve visibility and facilitate comparison.

signal plotted different β_z values for and Fig. 6.17 shows this for the species detected at m/z 127.

Fig. 6.16 shows only the m/z 125 species plotted with the β_z values of an ion with m/z 108 matches the SWIFT region. For a β_z of m/z 107 ($C_8H_{11}{}^+$), m/z 125 seems to dip where expected, however it rises at too high of a β_z. For m/z 109 and 110, m/z 125 dips and rises too early. The species at m/z 125 might form from m/z 127 and the m/z 125 with the β_z value of m/z 127 is shown to investigate if this is true. From that comparison, it is clear that m/z 125 dips and rises too early to be formed from m/z 127. Thus, m/z 125 matches the SWIFT region best when plotted with the β_z of m/z 108, which is shown in the main manuscript.

From Fig. 6.16 it can be seen that none of the β_z values other than that corresponding to m/z 109 make the dip of our species at m/z 127 match the SWIFT region. For a β_z of m/z 107 and 108, m/z 127 seems to dip and rise at too high β_z. For m/z 110, m/z 127 dips too early, although arguably it rises where expected. The m/z 127 species is plotted with the β_z value of m/z 125 to investigate a potential link between the two. We find that m/z 127 dips and rises too late to chemically link it with m/z 125. So, m/z 127 matches the SWIFT region best when plotted with the β_z of m/z 109, which is shown in the main manuscript.

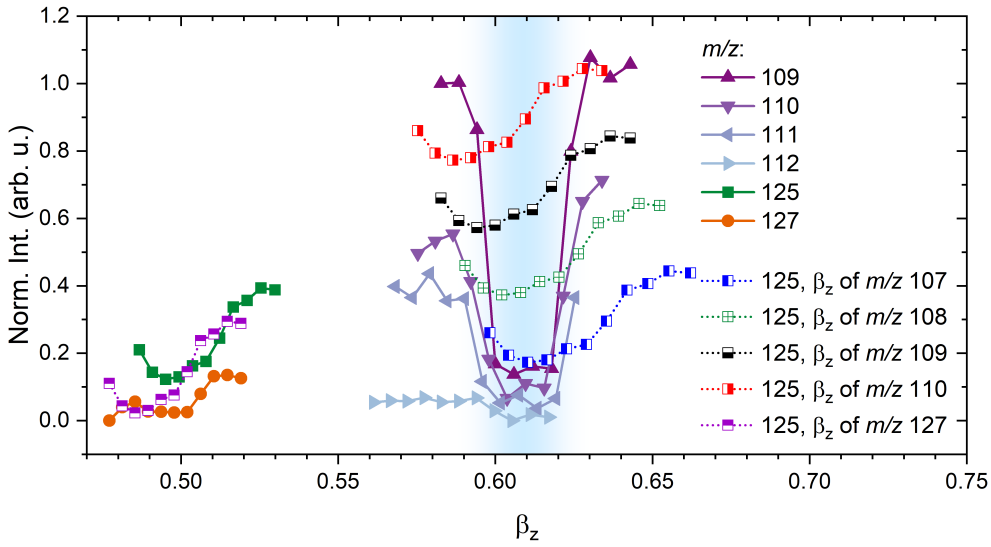

Figure 6.16: Integrated intensities of the C_9H^+ region as function of β_z. m/z 125 is plotted for different values of β_z (dotted line and half-filled square symbols),many of which are not presented in the main manuscript. The region where SWIFT was active is indicated by the blue shaded area. The data presented with the dotted lines is given a vertical offset to improve visibility and facilitate comparison.

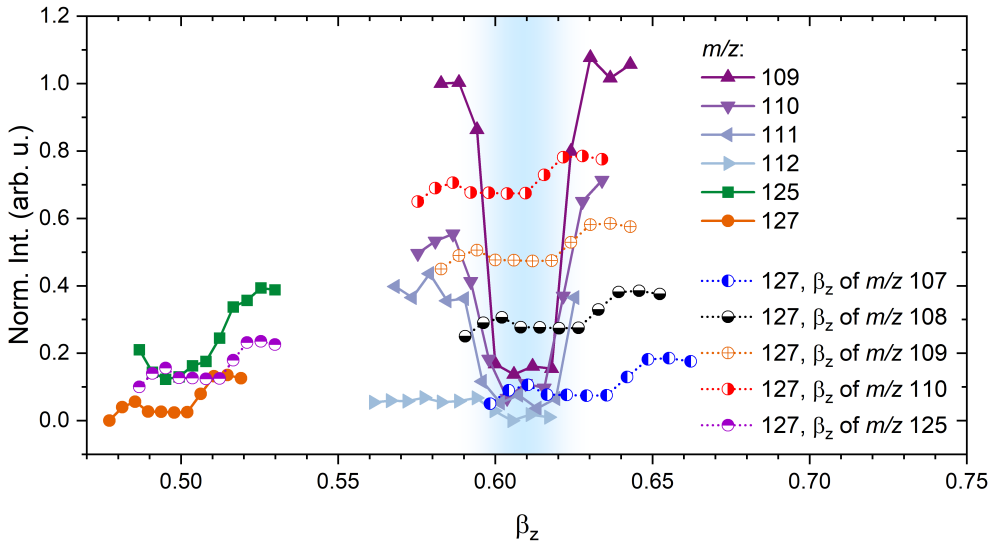

Figure 6.17: Integrated intensities of the C_9H^+ region as function of β_z. m/z 127 is plotted for different values of β_z (dotted line and half-filled circle symbols), many of which are not presented in the main manuscript. The region where SWIFT was active is indicated by the blue shaded area. The data presented with the dotted lines is given a vertical offset to improve visibility and facilitate comparison.